Spontaneous Hierarchical Assembly of Rhodium Nanoparticles into Spherical Aggregates and Superlattices

Trevor D. Ewers,[†] Amandeep K. Sra,[†] Brent C. Norris,[†] Robert E. Cable,[†] Chil-Hung Cheng,[‡] Daniel F. Shantz,[‡] and Raymond E. Schaak*[,†]

Departments of Chemistry and Chemical Engineering, Texas A&M University, College Station, Texas 77842-3012

Received September 17, 2004. Revised Manuscript Received October 25, 2004

Reduction of aqueous $RhCl_3$ with $NaBH_4$ in the presence of poly(vinyl pyrrolidone) (PVP) yields dense spherical nanostructures. The spherical aggregates, which generally have diameters between 10 and 100 nm, are built from smaller 1−3 nm Rh particles. The dense nanostructures are thermally stable beyond 100 °C, and they have a tendency to form ordered superstructures upon drying. Combining sodium *n*-dodecyl sulfate (SDS) with PVP modifies the size and morphology of the primary 1−3 nm particles, but does not change the spherical shape of the aggregates except at high concentrations of SDS. Small-angle X-ray scattering measurements show that the large aggregates are formed directly in solution from small Rh particles, consistent with TEM and AFM results. Magnetic measurements indicate that the Rh nanoparticle aggregates are Pauli paramagnetic.

Introduction

Controlling the synthesis[1,2] and assembly[1,3] of metal nanostructures is important for many applications, including catalysis,[4] nanoscale electronics,[5] and magnetic storage.[6] Methods that support hierarchical assembly over multiple length scales are particularly promising for designing functional nanostructures and assembling nanoscale devices. Many strategies for hierarchical assembly exist, and they often involve two distinct steps—synthesizing the appropriate precursors, and subsequently assembling them into larger structures. Examples of this approach include nanoparticle networks linked together using biological macromolecules[7] and biological recognition motifs,[8] mesoscopic superstructures assembled from amphiphilic nanorods,[9] crossed nanowire networks assembled using microfluidic and Langmuir−Blodgett techniques,[10] microscale shapes formed from nanoribbons[11] and platelets,[12] and hierarchical microstructures and functional circuits assembled from lithographically fabricated building blocks.[13]

In contrast to these multistep approaches, one-step strategies that combine synthesis with in-situ assembly are highly desired for their simplicity and for the robust structures that often form. Several reports in the past few years have shown that, under certain conditions, metal nanoparticles can spontaneously aggregate into larger spherical assemblies using a simple approach that combines synthesis and assembly in a one-step reaction.[14−18] These spongelike nanoparticle aggregates are robust, and often exhibit en-

* To whom correspondence should be addressed. E-mail: schaak@mail.chem.tamu.edu. Phone: (979) 458-2858. Fax: (979) 845-4719.
† Department of Chemistry.
‡ Department of Chemical Engineering.

(1) (a) Murray, C. B.; Kagan, C. R.; Bawendi, M. G. *Annu. Rev. Mater. Sci.* **2000**, *30*, 545−610. (b) Murray, C. B.; Sun, S.; Gaschler, W.; Doyle, H.; Betley, T. A.; Kagan, C. R. *IBM J. Res. Dev.* **2001**, *45*, 47−55.
(2) (a) Bonnemann, H.; Richards, R. M. *Eur. J. Inorg. Chem.* **2001**, 2455−2480. (b) Cushing, B. L.; Kolesnichenko, V. L.; O'Connor, C. J. *Chem. Rev.* **2004**, *104* (9), 3893−3946.
(3) Rogach, A. L.; Talapin, D. V.; Shevchenko, E. V.; Kornowski, A.; Haase, M.; Weller, H. *Adv. Funct. Mater.* **2002**, *12*, 653−664.
(4) (a) Gates, B. C. *Chem. Rev.* **1995**, *95*, 511−522. (b) Schlogl, R.; Hamid, S. B. A. *Angew. Chem., Int. Ed.* **2004**, *43*, 1628−1637.
(5) (a) Cui, Y.; Lieber, C. M. *Science* **2001**, *291*, 851−855. (b) Huang, Y.; Duan, X.; Cui, Y.; Lauhon, L. J.; Kim, K.-H.; Lieber, C. M. *Science* **2001**, *294*, 1313−1315. (c) Zhong, Z.; Wang, D.; Cui, Y.; Bockrath, M. W.; Lieber, C. M. *Science* **2003**, *302*, 1377−1380.
(6) (a) Sun, S.; Murray, C. B.; Weller, D.; Folks, A.; Moser, A. *Science* **2000**, *287*, 1989−1992. (b) Black, C. T.; Murray, C. B.; Sandstrom, R. L.; Sun, S. *Science* **2000**, *290*, 1131−1135.
(7) (a) Mirkin, C. A.; Letsinger, R. L.; Mucic, R. C.; Storhoff, J. J. *Nature* **1996**, *382*, 607−609. (b) Mucic, R. C.; Storhoff, J. J.; Mirkin, C. A.; Letsinger, R. L. *J. Am. Chem. Soc.* **1998**, *120*, 12674−12675. (c) Storhoff, J. J.; Mirkin, C. A. *Chem. Rev.* **1999**, *99*, 1849−1862.
(8) Lee, S.-W.; Mao, C.; Flynn, C. E.; Belcher, A. M. *Science* **2002**, *296*, 892−895.
(9) Park, S.; Lim, J.-H.; Chung, S.-W.; Mirkin, C. A. *Science* **2004**, *303*, 348−351.
(10) (a) Huang, Y.; Duan, X.; Wei, Q.; Lieber, C. M. *Science* **2001**, *291*, 630−633. (b) Whang, D.; Jin, S.; Wu, Y.; Lieber, C. M. *Nano Lett.* **2003**, *3*, 1255−1259. (c) Jin, S.; Whang, D.; McAlpine, M. C.; Friedman, R. S.; Wu, Y.; Lieber, C. M. *Nano Lett.* **2004**, *4*, 915−919.
(11) Liu, B.; Zeng, H. C. *J. Am. Chem. Soc.* **2004**, *126*, 8124−8125.
(12) Yuan, J.; Laubernds, K.; Zhang, Q.; Suib, S. L. *J. Am. Chem. Soc.* **2003**, *125*, 4966−4967.
(13) (a) Bowden, N. B.; Weck, M.; Choi, I. S.; Whitesides, G. M. *Acc. Chem. Res.* **2001**, *34*, 231−238. (b) Wu, H.; Thalladi, V. R.; Whitesides, S.; Whitesides, G. M. *J. Am. Chem. Soc.* **2002**, *124*, 14495−14502.
(14) Liang, H.-P.; Zhang, H.-M.; Hu, J.-S.; Guo, Y.-G.; Wan, L.-J.; Bai, C.-L. *Angew. Chem., Int. Ed.* **2004**, *43*, 1540−1543.
(15) Ely, T. O.; Amiens, C.; Chaudret, B.; Snoeck, E.; Verelst, M.; Respaud, M.; Broto, J.-M. *Chem. Mater.* **1999**, *11*, 526−529.
(16) (a) Vidoni, O.; Philippot, K.; Amiens, C.; Chaudret, B.; Balmes, O.; Malm, J.-O.; Bovin, J.-O.; Senocq, F.; Casanove, M.-J. *Angew. Chem., Int. Ed.* **1999**, *38*, 3736−3738. (b) Pelzer, K.; Vidoni, O.; Philippot, K.; Chaudret, B.; Colliere, V. *Adv. Funct. Mater.* **2003**, *13*, 118−126.
(17) Song, Y.; Yang, Y.; Medforth, C. J.; Pereira, E.; Singh, A. K.; Xu, H.; Jiang, Y.; Brinker, C. J.; van Swol, F.; Shelnutt, J. A. *J. Am. Chem. Soc.* **2004**, *126*, 635−645.

10.1021/cm0483792 CCC: $30.25 © 2005 American Chemical Society
Published on Web 01/12/2005

hanced properties relative to both discrete nanoparticles and bulk powders. For example, Liang et al. recently reported the synthesis of hollow sphere aggregates of Pt nanoparticles by templating against a sacrificial Co nanoparticle core, and dense analogues could also be formed using a multistep seeded growth strategy.[14] Importantly, the hollow sphere nanoparticle aggregates show enhanced electrocatalytic activity.[14] Chaudret and co-workers described the spontaneous formation of spherical Ni nanoparticle aggregates, which showed interesting magnetic properties and assembled into linear superstructures.[15] The same group also reported similar spongelike Ru nanoparticles that are catalytically active.[16] Shelnutt and co-workers reported spherical dendritic structures that form from the surfactant-assisted reduction and autocatalytic growth of Pt.[17] Heterogeneous bimetallic Au−Pt nanoparticle aggregates of similar morphology were also formed using a multi-stage growth strategy.[18] In many cases, the spontaneous assembly of metal nanoparticles into spherical aggregates is unexpected, but the resulting nanomaterials possess interesting structures and properties.

There has been a significant amount of research describing the synthesis of metal nanoparticles of the late transition metals in recent years.[2] However, much of this work has focused on synthesizing nanoparticles of Co, Pd, Pt, Ag, and Au. A search of the literature confirms that the synthesis of Rh nanoparticles has received much less attention. Because of their potential use as catalysts[4,19] and their potentially interesting optical[20] and magnetic[21−23] properties, we were interesting in exploring methods for synthesizing Rh nanoparticles and exploring their assembly into complex structures. During our attempts to synthesize Rh nanoparticles stabilized by poly(vinylpyrrolidone) (PVP) using an approach that is well-established for late transition metal systems,[2,24−26] we discovered that dense spherical aggregates form instead of discrete nanoparticles. Accordingly, we report here the synthesis and spontaneous hierarchical assembly of rhodium nanoparticles into uniform spherical aggregates and superlattices using a one-step reaction. The aggregates are surprisingly dense and uniform, and they spontaneously order over several length scales. These spherical aggregates have the potential to be important building blocks for more complex nanostructures, and are also potentially interesting for magnetic studies and catalytic applications.

Experimental Section

Spherical aggregates of Rh nanoparticles stabilized by PVP were synthesized by the one-step borohydride reduction of dilute aqueous $RhCl_3$. Briefly, $RhCl_3$ (24 mg) and PVP of various molecular weights and quantities (MW = 8000, 40 000, 630 000; mass = 230, 920, 1380 mg) were dissolved in 50 mL of deionized distilled water (NANOpure, 18.2 MΩ). Then, $NaBH_4$ (10 mg) dissolved in 5 mL of water was added to the $RhCl_3$/PVP solution with constant stirring, and stirring was allowed to continue for 30 min. The resulting Rh nanoparticle aggregates were isolated by centrifugation and washed several times with ethanol. In some cases, sodium *n*-dodecyl sulfate (SDS) was used instead of or in addition to PVP.

Transmission electron microscopy (TEM) images and selected area electron diffraction (SAED) patterns were acquired using a JEOL JEM-2010 TEM. Samples for TEM analysis were prepared by re-suspending the Rh nanoparticle aggregates in ethanol and depositing them onto a carbon-coated Cu grid. Powder X-ray diffraction (XRD) data were collected on a Bruker GADDS three-circle diffractometer using Cu Kα radiation. Peak broadening was analyzed using the Scherrer equation to determine the coherence length of the nanocrystals. Corrections for instrumental broadening were made using bulk Rh metal as a standard. UV−Visible spectra were collected on a Jasco V-530 UV−visible spectrophotometer. Elemental analysis (CHN) was performed by Atlantic Microlab (Norcross, GA).

Atomic force microscopy (AFM) images were obtained in tapping mode in air using a Digital Instruments Nanoscope III AFM fitted with a 200-mm j-scanner. Tapping mode cantilevers (MikroMasch) had resonant frequencies between 265 and 400 kHz (typical 325 kHz), force constants of 20−75 N/m, and tip apex radii of ∼10 nm. Images were acquired at 512 × 512 pixels and 0.75 Hz using a near-minimal contacting force. The resulting images were flattened and plane-fit using Digital Instruments software.

Magnetic susceptibility and magnetization measurements were carried out on a Quantum Design SQUID magnetometer MPMS-XL. Measurements were performed in dc mode from 2 to 300 K with an applied field of 1000 Oe.

Small-angle X-ray scattering (SAXS) measurements were performed on a Bruker NanoSTAR system with a Nonius rotating anode (FR591) and a copper target (1.5417 Å) operating at 45 kV and 90 mA. Incident beam collimation was achieved using cross-coupled Goebel mirrors and three pinholes. The scattering intensity was measured on a two-dimensional multiwire Hi-STAR detector and the residual direct beam was blocked by a beam stop. The whole system was operated under vacuum (10^{-2} mbar). The sample-to-detector distance was 64 cm, corresponding to a q range of approximately 0.02−0.3 $Å^{-1}$ ($q = 4\pi\sin(\theta)/\lambda$, where θ is half of the scattering angle and λ is the wavelength of the incident beam). Samples were measured in 1-mm-diameter quartz capillaries and mounted in an Anton Paar HR−PHK sample chamber. The scattered intensity of the particles was calculated using toluene as the reference material for the background subtraction in data analysis. The scattering data were analyzed using the program *GNOM*[27] to determine the pair distance distribution function (PDDF) using the inverse Fourier transform method.[28−31] Full-profile fitting was also performed using a least-squares method described by Pederson.[32]

(18) Schmid, G.; Lehnert, A.; Malm, J.-O.; Bovin, J.-O. *Angew. Chem., Int. Ed.* **1991**, *30*, 874−876.
(19) Rupprechter, G.; Hayek, K.; Hofmeister, H. *Nanostruct. Mater.* **1997**, *9*, 311−314.
(20) (a) Papavassiliou, G. C. *Prog. Solid State Chem.* **1979**, *12*, 185−271. (b) Mulvaney, P. *Langmuir* **1996**, *12*, 788−800.
(21) Cox, A. J.; Louderback, J. G.; Bloomfield, L. A. *Phys. Rev. Lett.* **1993**, *71*, 923−926.
(22) Cox, A. J.; Louderback, J. G.; Apsel, S. E.; Bloomfield, L. A. *Phys. Rev. B* **1994**, *17*, 12295−12298.
(23) (a) Berlanga-Ramirez, E. O.; Aguilera-Granja, F.; Diaz-Ortiz, A.; Rodriguez-Lopez, J. L.; Vega, A. *J. Alloys Compd.* **2004**, *369*, 81−83. (b) Huger, E.; Osuch, K. *Solid State Commun.* **2004**, *131*, 175−179.
(24) Brown, H. C.; Brown, C. A. *J. Am. Chem. Soc.* **1962**, *84*, 1493−1494.
(25) Bonnemann, H.; Brijoux, W.; Brinkmann, R.; Fretzen, R.; Joussen, T.; Koppler, R.; Korall, B.; Neiteler, P.; Richter, J. *J. Mol. Catal.* **1994**, *86*, 129−177.
(26) Lu, W.; Wang, B.; Wang, K.; Wang, X.; Hou, J. G. *Langmuir* **2003**, *19*, 5887−5891.
(27) Svergun, D. I. *J. Appl. Crystallogr.* **1992**, *25*, 495−503.
(28) Glatter, O. *J. Appl. Crystallogr.* **1977**, *10*, 415−421.
(29) Glatter, O. *J. Appl. Crystallogr.* **1979**, *12*, 166−173.
(30) Glatter, O. *J. Appl. Crystallogr.* **1980**, *13*, 7−11.
(31) Glatter, O. *J. Appl. Crystallogr.* **1980**, *13*, 577−584.
(32) Pedersen, J. S. *Adv. Colloid Interface Sci.* **1997**, *70*, 171−210.

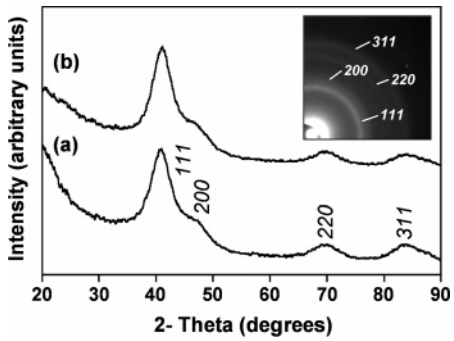

Figure 1. Powder XRD patterns for Rh nanoparticle aggregates prepared using (a) 920 mg of PVP (MW = 40 000) and (b) 920 mg of PVP and 1.01 g of SDS. The inset shows the SAED pattern for the spherical nanoparticle aggregates formed using PVP.

Results and Discussion

Synthesis and Assembly of Spherical Aggregates of Rhodium Nanoparticles. We initially attempted to synthesize PVP-stabilized Rh nanoparticles by borohydride reduction in a manner similar to that used by Lu et al. to synthesize amorphous Pd nanoparticles.[26] Upon addition of aqueous $NaBH_4$ to a solution of $RhCl_3$ and PVP (MW = 40 000) in water, the color immediately changed from orange-red to black, suggesting that reduction occurred. The nanoparticle solution was stable for weeks without noticeable precipitation. However, the product could be isolated easily by centrifugation at low speeds, which was surprising and suggested the presence of large Rh particles. XRD data for the precipitate are shown in Figure 1. The peak positions match well with those expected for fcc Rh, and the peak broadening indicates that the crystallites are small. Particle size analysis using the Scherrer equation[33] yielded an average crystallite size of 2.6 nm.

Because discrete 2−3-nm particles would not be expected to precipitate rapidly during centrifugation at 10 000 rpm, we speculated that large aggregates of nanoparticles formed. TEM micrographs for the Rh nanoparticle aggregates are shown in Figure 2. The low-resolution TEM micrograph in Figure 2a shows large spherical particles that range in diameter from 12 to 70 nm. The high-resolution image in Figure 2b shows that the large spherical particles are comprised of densely packed 1−3 nm nanocrystals. The nanocrystal aggregates are surprisingly spherical, although their diameters span a range of sizes. A histogram of particle size distributions summarizing the analysis of approximately 200 spherical aggregates is shown in Figure 3a. Statistical analysis yielded an average diameter of 53 ± 18 nm. The percent yield of spherical nanoparticle aggregates, based on analysis of all TEM images from this and related samples, is ∼100%. Elemental analysis (CHN) confirms that PVP remains attached to the nanoparticle surface, with an average Rh:PVP ratio of 8.6:1 (w/w) in the washed and dried sample.

To confirm that the nanoparticle aggregates are spherical and not flat (which can be difficult to discern by TEM), we dried a dilute suspension on a clean Si surface and analyzed the heights of the aggregates using AFM. The AFM image, shown in Figure 4, confirms that the aggregates are spherical as deposited on the surface. Height profile analysis (Sup-

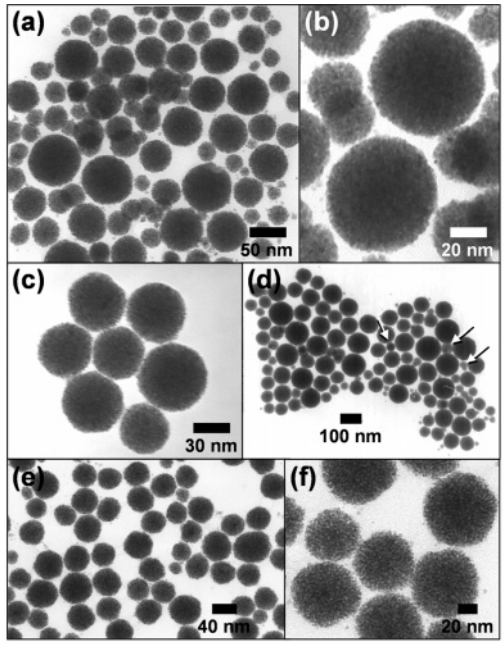

Figure 2. TEM micrographs of spherical Rh nanoparticle aggregates synthesized using 920 mg of PVP (MW = 40 000) are shown in (a) and (b). Panel (c) shows a hexagonal superlattice, and panel (d) shows a superlattice formed after drying a suspension that was size-focused by centrifugation at 1000 rpm. The arrows in (d) point to small spheres that sit in interstitial sites formed by larger spheres. A submonolayer of spherical aggregates deposited on a TEM grid and heated to 100 °C is shown in (e) and (f).

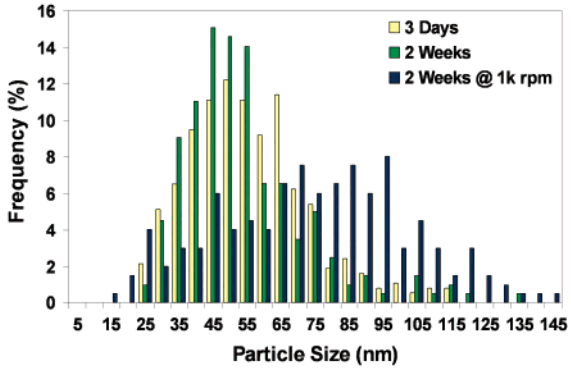

Figure 3. Particle size distribution histograms for spherical Rh nanoparticle aggregates synthesized using 920 mg of PVP (MW = 40 000) and stirred for (a) 3 days (yellow) and (b) two weeks (green). The size distribution histogram for the sample stirred for two weeks and then centrifuged (size-focused) at 1000 rpm is shown in blue (c).

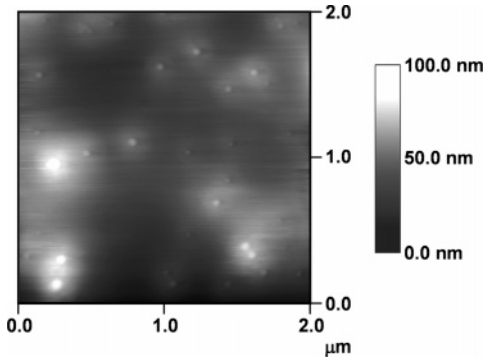

Figure 4. AFM image of spherical Rh nanoparticle aggregates deposited on a clean Si wafer.

(33) Klug, H. P.; Alexander, L. E. *X-ray Diffraction Procedures*; John Wiley: New York, 1959.

Table 1. Summary of Results from XRD and TEM Analyses

PVP molecular weight (g/mol)	mass PVP (mg)	mass SDS (mg)	primary particle size by XRD (nm)	primary particle size by TEM (nm)	spherical aggregate size by TEM (nm)
8000	920	0	2.6	1−3	46 ± 21
40 000	230	0	3.0	1−3	34 ± 13
40 000	920	0	2.6	1−3	53 ± 18
40 000	1380	0	2.4	1−3	39 ± 21
630 000	920	0	2.0	1−3	50 ± 13
630 000	920	200	3.0	1−3	35 ± 7
630 000	920	1010	2.3	3−5	33 ± 4
630 000	0	1010	3.0	2−7	N/A

porting Information) shows that the spherical aggregates are approximately as tall as they are wide, within experimental error. Typical height values were 20−60 nm, and typical diameters were 40−100 nm. Due to tip broadening effects for these small features, the sphere diameters can appear wider than they actually are. The halos surrounding the spherical aggregates may be due to excess polymer that dried on the surface, tip effects, or the process of flattening the image.

The morphology of spherical Rh aggregates is similar to that of Ni nanoparticle aggregates reported by Chaudret and co-workers, who also used PVP as a surface stabilizing polymer.[15] In their work, solvent and polymer chain length were found to influence the formation of the superstructures.[15] To more carefully study this dependence for our Rh sample, we systematically varied the concentration and molecular weight of the PVP, as well as the solvent and type of surface stabilizing agent. Table 1 summarizes the results that are discussed below.

PVP with different molecular weights (MW = 8000, 40 000, 630 000) produced Rh nanoparticle aggregates with the same spherical morphology. For low molecular weight PVP (MW = 8000), the average diameter of the nanoparticle aggregates was 46 ± 21 nm. Particle size analysis of the XRD data for this sample showed a crystallite size of 2.6 nm. Likewise, high molecular weight PVP (MW = 630 000) produced spherical aggregates with an average diameter of 50 ± 13 nm and a crystallite size of 2.0 nm. In contrast to the Ni nanoparticle aggregates, the molecular weight of PVP does not significantly influence the formation of Rh nanoparticle aggregates or their morphology.

We also studied the effect on morphology of varying the relative concentrations of metal and PVP; the metal concentration remained constant, and the PVP concentration was varied. Again, spherical nanoparticle aggregates were observed in all cases. For 230, 920, and 1380 mg of PVP (MW = 40 000), the average diameters of the spherical aggregates were 34 ± 13, 53 ± 18, and 39 ± 21 nm, respectively. There is no systematic trend in the average sizes of the nanoparticle aggregates (and they are all generally within one standard deviation of each other), and we attribute this range in average sizes to uncontrollable sample-to-sample variation. The percent yields of spherical nanoparticle aggregates for the samples where PVP molecular weight and concentration were varied are all near 95%.

The size distribution can be changed by centrifuging at low speeds. A TEM micrograph of spherical nanoparticle aggregates synthesized using 920 mg of PVP (MW = 40 000) and size-focused by centrifuging at 1000 rpm is shown in Figure 2d. The particle size distribution histogram in Figure 3c confirms that a range of sizes is still present, but the size distribution has been shifted to larger diameters. Indeed, the average diameter for the centrifuged sample is 73 ± 28 nm, compared to 52 ± 19 nm for the as-made sample.

Because the nanoparticle aggregates are highly spherical, they tend to organize into close-packed superstructures upon solvent evaporation. For example, a hexagonal array of spherical aggregates prepared using 920 mg of PVP (MW = 40 000) is shown in Figure 2c. The size-focused sample in Figure 2d also shows signs of higher-order organization: smaller spheres tend to fall in interstitial sites between larger spheres (see arrows in Figure 2d). With further purification and size-selection, it may be possible to assemble larger arrays of uniform spherical aggregates, or also to form bimodal mixtures of spheres that organize into binary superlattices.

As shown in the histogram in Figure 3, the reaction time (e.g., stirring time) does not have a measurable effect on the size distribution of the nanoparticle aggregates. However, all attempts to form spherical nanoparticle aggregates in different solvents (e.g., ethanol, ethylene glycol) failed; only discrete nanocrystals were formed. Apparently, the solvent is important for stabilizing the spherical aggregates. This may be due to solvent−polymer interactions that change its conformation and mobility in solution in a way that modifies its ability to induce nanoparticle aggregation.

Interestingly, the spherical nanostructures are thermally stable. Figure 2e shows spherical aggregates of Rh nanoparticles heated to 100 °C after deposition on a TEM grid. The TEM micrograph shows that the aggregates remain dense, spherical, and discrete. The expanded view in Figure 2f confirms that the primary nanoparticles remain intact, although some grain growth occurs. The crystallite sizes, determined from TEM analysis, range from 2 to 4 nm.

Influence of Polymer−Surfactant Mixtures on Morphology. It is known that PVP has structural interactions with many surfactants, including SDS.[34,35] These interactions can cause changes in the critical micelle concentrations of the surfactants, the structures of the mesophases that form, and the flexibility and conformation of the polymer chains.[34] Thus, we were interested in studying the influence of SDS and SDS/PVP interactions on the formation of spherical nanoparticle aggregates.

A reaction containing 200 mg of SDS and 920 mg of PVP (MW = 630 000) produced spherical nanoparticle aggregates with an average size of 35 ± 7 nm. This size distribution is narrower than that of samples prepared using only PVP. However, the TEM micrograph in Figure 5a shows that the primary Rh nanoparticles are larger than those prepared using

(34) Jonsson, B.; Lindman, B.; Holmberg, K.; Kronberg, B. *Surfactants and Polymers in Aqueous Solution*; John Wiley: Chichester, 1998.
(35) (a) Sesta, B.; D'Aprano, A.; Segre, A. L.; Proietti, N. *Langmuir* **1997**, *13*, 6612−6617. (b) Purcell, I. P.; Lu, J. R.; Thomas, R. K.; Howe, A. M.; Penfold, J. *Langmuir* **1998**, *14*, 1637−1645. (c) Griffiths, P. C.; Hirst, N.; Paul, A.; King, S. M.; Heenan, R. K.; Farley, R. *Langmuir* **2004**, *20*, 6904−6913.

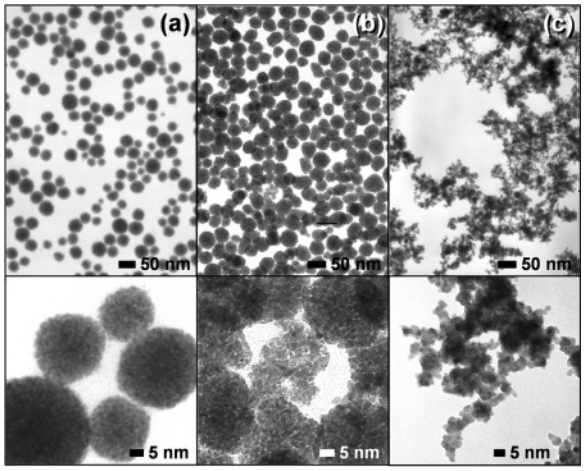

Figure 5. TEM micrographs for Rh nanoparticles synthesized using (a) 920 mg of PVP (MW = 40 000) and 200 mg of SDS, (b) 920 mg of PVP and 1.01 g of SDS, and (c) 1.01 g of SDS without PVP.

only PVP. In contrast, the XRD data in Figure 1b yields a particle size of 3.0 nm. Using 1.01 g of SDS and 920 mg of PVP also yielded spherical nanoparticle aggregates (Figure 5b) with an average size of 33 ± 4 nm. The crystallite sizes for this sample are 3−5 and 2.3 nm as determined from TEM and XRD analysis, respectively. The average crystallite size remains the same based on XRD, while TEM analysis shows that the primary particles grow larger with increasing SDS concentration. This suggests that the primary Rh nanoparticles in the SDS/PVP aggregates are polycrystalline.

Overall, the SDS/PVP sample is highly monodisperse, and large-area superlattices are prevalent (Figure 5b). However, several regions showed discrete nanoparticles and nonspherical aggregates (Figure 5b). Using only SDS and no PVP yielded randomly shaped networks of discrete nanoparticles (Figure 5c) with particle sizes of 3.0 nm and 2−7 nm as determined from XRD and TEM analysis, respectively. The percent yields of *spherical* nanoparticle aggregates systematically decreased as more SDS was added: approximately 100%, 90%, 70%, and 0% for 920 mg of PVP, 920 mg of PVP/200 mg of SDS, 920 mg of PVP/1.01 g of SDS, and 1.01 g of SDS, respectively. This confirms that PVP is necessary for forming the spherical aggregates. Furthermore, it suggests that SDS plays a role in forming the primary nanoparticle building blocks, while PVP (or perhaps other similar polymers) is responsible for assembling the nanoparticles into spherical aggregates. Mechanistic studies of the formation of PVP-stabilized nanoparticles and their aggregates are consistent with this observation,[36] and suggest that the particles are held together by attachment to the polymer chains.

Small-Angle X-ray Scattering. One of the most interesting aspects of this work is that the Rh nanoparticles aggregate spontaneously into spherical assemblies in solution. To confirm that the spherical aggregates exist in solution rather than forming postsynthesis as an artifact of drying, we used SAXS to study the morphology and size distribution of the as-synthesized samples directly in solution.

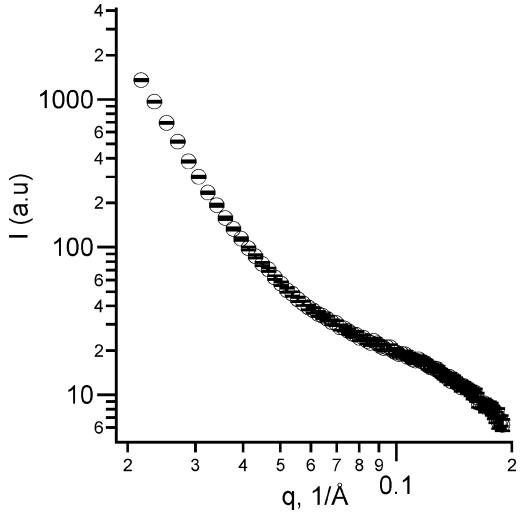

Figure 6. SAXS data for Rh nanoparticle aggregates prepared using 920 mg of PVP (MW = 40 000).

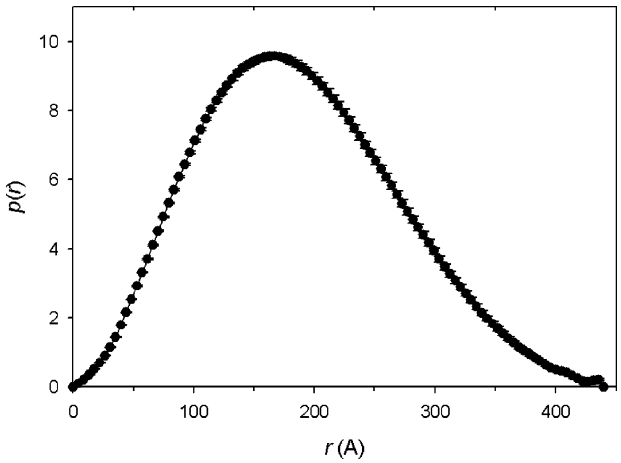

Figure 7. Pair distance distribution function, $p(r)$, for the Rh nanoparticle aggregates.

Figure 6 shows the SAXS results for a typical sample. In both of the q ranges between 0.02−0.05 Å^{-1} and 0.1−0.2 Å^{-1} the slope in the plot of *log I* verus *log q* is −4, consistent with spherical scatterers. Guinier analysis[37] of the low q data yields a radius of gyration (R_g) of 140 Å, which in the case of spherical particles gives a particle diameter of 360 Å. The particle size calculated from the pair distance distribution function (pddf), or $p(r)$, which is given by the equation

$$p(r) = \frac{1}{(2\pi^2)}\int_0^\infty I(q)qr\sin(qr)dq$$

is consistent with that of Guinier analysis, and indicates polydisperse spherical particles with a mean radius of 185 Å (Figure 7). However, the change in slope between 0.05 and 1 Å^{-1} indicates that there is a second particle population, which will be shown below to be the primary 1−2 nm Rh particles that form the larger aggregates. Consistent with this, full-profile fitting assuming a normal distribution of spherical particles could not account for the scattering behavior above 0.05 Å^{-1} (Supporting Information). Also, consistent with the TEM results, the large ∼40-nm spherical aggregates are

(36) (a) Pastoriza-Santos, I.; Liz-Marzan, L. M. *Langmuir* **2002**, *18*, 2888−2894. (b) Shin, H. S.; Yang, H. J.; Kim, S. B.; Lee, M. S. *J. Colloid Interface Sci.* **2004**, *274*, 89−94.

(37) Guinier, A.; Fournet, G. *Small-Angle Scattering of X-rays*; John Wiley: New York, 1955.

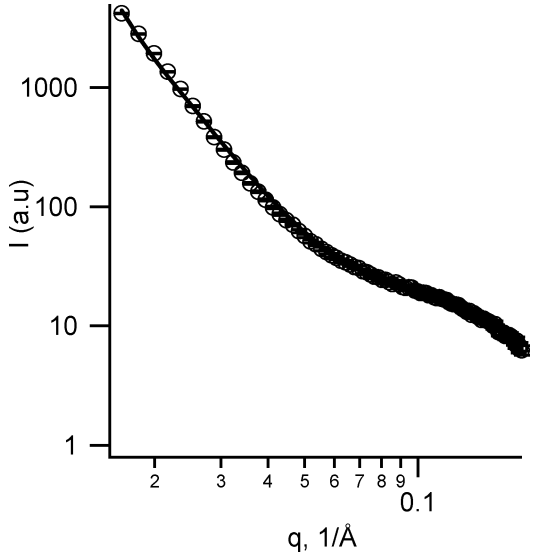

Figure 8. Full-profile fitting of the SAXS data (solid line) using the parameters listed in Table 2.

Table 2. Results from Full-Profile Fitting of the SAXS Data

Rh spherical aggregates		Rh primary particles	
mean radius (Å)	standard deviation (Å)	mean radius (Å)	standard deviation (Å)
180	60	10	2

polydisperse ($\sigma/r \geq 0.3$) based on the complete absence of oscillations in the scattering data between 0.02 and 0.1 $Å^{-1}$. To successfully fit the full scattering curve, a second population of particles with a mean radius of 10 Å had to be included in the full-profile fitting. Figure 8 shows the full-profile fit assuming a bimodal size distribution, and Table 2 includes the fit parameters. No feature indicative of particles with a radius of approximately 10 Å is observed in the pddf, (e.g., a maximum), and this is consistent with the observation that the large particles are formed by aggregates of these small particles. The one minor shortcoming of the full-profile fitting is that the small oscillations observed in the fit in the q range 0.02−0.06 $Å^{-1}$ are not observed in the experimental data. This is again due to the polydispersity of the sample. The SAXS data clearly show that the large Rh aggregates, on average 36 nm in diameter, are spherical and that they exist in solution as synthesized. Furthermore, the SAXS data confirm that the large spherical aggregates are comprised of smaller particles with an average diameter of 2 nm. These results are in agreement with the TEM, XRD, and AFM studies.

Optical and Magnetic Properties. Figure 9 shows UV−visible absorption data for several samples of Rh nanoparticle aggregates. The absorption spectra are relatively featureless, and the broad and overall constant low absorbance over the visible region is consistent with the black color of the aggregates. The Rh:PVP ratio does not influence the absorption spectra, and this is consistent with the structure and morphology studies. Likewise, the spectrum for the PVP/SDS sample is similar to the others. Notably, there are no well-defined plasmon bands evident in any of the spectra, and this is most likely because of the small size of the primary Rh nanoparticles (2−3 nm) that comprise the larger

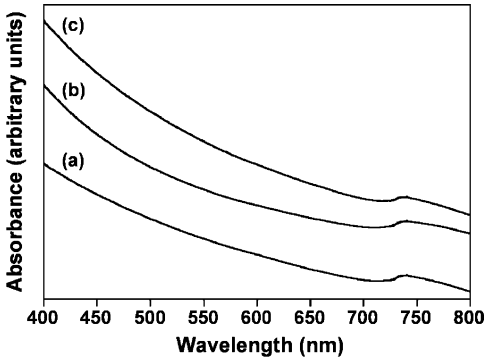

Figure 9. Visible absorption spectra for dilute aqueous solutions of spherical Rh nanoparticle aggregates synthesized using (a) 230 mg of PVP (MW = 40 000), (b) 1380 mg of PVP, and (c) 920 mg of PVP and 200 mg of SDS.

spherical aggregates. It is well-known that small nanoparticles have significantly broadened plasmon bands, and particles in this size range have plasmon bands that are sufficiently broadened that they are not evident in absorption spectra.[38]

While rhodium is considered to be a nonmagnetic metal, it is more accurately classified as Pauli paramagnetic, since its conduction electrons respond paramagnetically to an applied field. Bulk rhodium is not ferromagnetic. However, giant magnetic moments associated with ferromagnetic ordering were observed in small Rh clusters,[21,22] and these observations agree well with theoretical studies.[23,39] Magnetism in small clusters of other nonmagnetic elements, such as Pd and Pt, have also been studied experimentally[40] and theoretically.[41] For the magnetic Rh clusters, the moment disappears for clusters larger than approximately 1 nm.[22] Because our spherical nanoparticle aggregates are comprised of small 1−3 nm particles that are near this limit of magnetism, we were interested in studying their magnetic properties.

Temperature-dependent dc susceptibility data at 1000 Oe for a representative sample of spherical Rh nanoparticle aggregates, along with bulk Rh metal, are shown in Figure 10. Bulk Rh metal shows a small positive temperature-independent susceptibility, consistent with the expected Pauli paramagnetism. The magnetic susceptibility of the Rh nanoparticle aggregates is similar to that of bulk Rh, appearing nearly temperature-independent with a small positive susceptibility. The paramagnetic tail at low temperatures is typical for trace amounts of magnetic impurities, which we attribute to unavoidable impurities from the reagents used during the solution synthesis. The magnitude of the positive susceptibility for the Rh nanoparticle aggregates is somewhat larger than that for bulk Rh, which could result from the small size of the nanoparticles or from defects in the structure

(38) Lisiecki, I.; Pileni, M. P. *J. Phys. Chem.* **1995**, *99*, 5077−5082.
(39) (a) Blugel, S. *Phys. Rev. Lett.* **1992**, *68*, 851−854. (b) Reddy, B. V.; Khanna, S. N.; Dunlap, B. I. *Phys. Rev. Lett.* **1993**, *70*, 3323−3326.
(40) (a) Sampedro, B.; Crespo, P.; Hernando, A.; Litran, R.; Sanchez Lopez, J. C.; Lopez Cartes, C.; Fernandez, A.; Ramirez, J.; Gonzalez Calbet, J.; Vallet, M. *Phys. Rev. Lett.* **2003**, *91*, 237203. (b) Kim, Y. N.; Lee, E. K.; Lee, Y. B.; Shim, H.; Hur, N. H.; Kim, W. S. *J. Am. Chem. Soc.* **2004**, *126*, 8672−8673.
(41) (a) Vitos, L.; Johansson, B.; Kollar, J. *Phys. Rev. B* **2000**, *62*, R11957−11960. (b) Delin, A.; Tosatti, E.; Weht, R. *Phys. Rev. Lett.* **2004**, *92*, 057201.

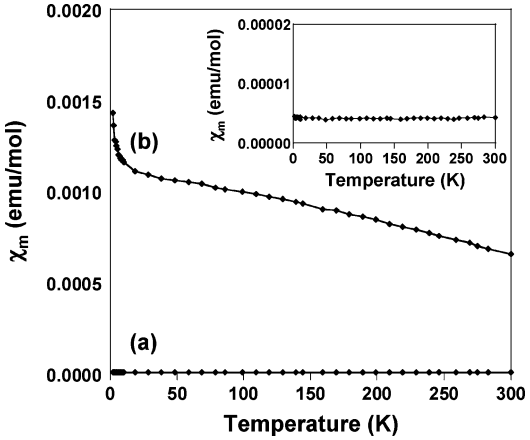

Figure 10. Field-cooled dc susceptibility data for (a) bulk Rh metal and (b) spherical Rh nanoparticle aggregates from 4 to 300 K at 1000 Oe. Inset: dc susceptibility for bulk Rh metal [sample (a)] on a different scale to show its positive susceptibility.

or surface of the nanoparticles. PVP generally does not have a significant influence on the magnetic properties of nanoparticles.[15,42] However, surface effects are not uncommon, and these can lead to enhanced moments.[43]

The spherical Rh nanoparticle aggregates are clearly not ferromagnetic, and this is most likely because the primary nanoparticles are larger than the threshold size necessary for ferromagnetism to occur.[22] If synthetic routes could be developed to yield smaller primary nanoparticles (e.g., by more careful control over polymer−surfactant mixtures), it may be possible to synthesize spherical assemblies with sufficiently small Rh nanoparticles to induce ferromagnetism. Such materials would be interesting for studying the effect of assembly and mesostructure on cooperative magnetic phenomena.

Conclusions

In this paper, we have established that PVP-stabilized Rh nanoparticles spontaneously aggregate into dense spherical nanostructures in solution. These spherical aggregates, which generally have diameters between 10 and 100 nm, are built from smaller 1−3 nm particles and form without the need for seed-mediated or electrochemical growth. The dense nanostructures are thermally stable, and they have a tendency to form ordered superstructures upon drying. This system supports spontaneous hierarchical organization over three length scales, which suggests that more complex nanostructures may be accessible by optimizing the synthesis and purification processes to achieve higher monodispersity. While nanoparticle aggregates of Pt,[14,17] Ni,[15] Ru,[16] Au−Pt,[18] and some oxides[44] have been reported previously, this work represents the first example of Rh forming similar nanostructures. This is particularly important considering the known catalytic activity of nanoscale Rh[4,19] and the exotic magnetic phenomena that can be achieved with small clusters of Rh and other nonmagnetic 4d and 5d transition elements.[21−23,39−41] Along those lines, these well-defined nanoparticle aggregates could be important systems for studying the influence of catalytic activity and cooperative magnetic properties on interparticle separation and nanostructure, since other similar aggregated structures have proven to exhibit enhanced properties relative to those of their discrete nanoparticles and bulk powders.

Acknowledgment. R.E.S. acknowledges Texas A&M University and the Robert A. Welch Foundation (Grant A-1583) for support. R.E.S. also acknowledges the Donors of the American Chemical Society Petroleum Research Fund for partial support of this research. D.F.S. acknowledges support from Texas A&M University. Electron microscopy was performed at the Microscopy and Imaging Center at Texas A&M University, and AFM images were acquired at the TAMU/CIMS Materials Characterization Facility. We thank Francois Gabbai for use of the UV-visible spectrophotometer. The small-angle X-ray scattering instruments were obtained with funds provided by the National Science Foundation under Grant 0215838. The SQUID magnetometer was obtained with funds provided by a National Science Foundation equipment grant (NSF-9974899).

Supporting Information Available: SAXS data and simulated scattering curve for spheres with a normal size distribution, TEM micrograph of large-area superlattice, and AFM cross section analysis (PDF). This material is available free of charge via the Internet at http://pubs.acs.org.

CM0483792

(42) (a) Hou, Y.-L.; Gao, S. *J. Alloys Compd.* **2004**, *365*, 112−116. (b) Jeong, J.-R.; Choi, M. C.; Kim, M. W.; Shin, S.-C. *Phys. Status Solidi B* **2004**, *241*, 1609−1612.

(43) (a) Osuna, J.; de Caro, D.; Amiens, C.; Chaudret, B.; Snoeck, E.; Respaud, M.; Broto, J.-M.; Fert, A. *J. Phys. Chem.* **1996**, *100*, 14571−14574. (b) Respaud, M.; Broto, J. M.; Rakato, H.; Fert, A. R.; Thomas, L.; Barbara, B.; Verelst, M.; Snoeck, E.; Lecante, P.; Mosset, A.; Osuna, J.; Ould Ely, T.; Amiens, C.; Chaudret, B. *Phys. Rev. B* **1998**, *57*, 2925−2935.

(44) (a) Euliss, L. E.; Grancharov, S. G.; O'Brien, S.; Beming, T. J.; Stucky, G. D.; Murray, C. B.; Held, G. A. *Nano Lett.* **2003**, *3*, 1489−1493. (b) He, T.; Chen, D.; Jiao, X. *Chem. Mater.* **2004**, *16*, 737−743.